

Supporting Information

Engineering On-Chip Nanoporous Gold Material Libraries via Precision Photothermal Treatment

*Christopher A. R. Chapman^a, Ling Wang^b, Juergen Biener^c, Erkin Seker^b, Monika M. Biener^c,
and Manyalibo J. Matthews^{c*}*

a) Department of Biomedical Engineering, University of California – Davis, Davis, CA 95616

*b) Department of Electrical and Computer Engineering, University of California – Davis, Davis,
CA 95616*

c) Lawrence Livermore National Laboratory, Livermore, CA 94551

**corresponding author, ibo@llnl.gov*

Chemicals and Materials: Gold, silver, and chrome targets (99.95% pure) were obtained from Kurt J. Lesker. Polydimethylsiloxane (PDMS) sheets were obtained from B&J rubber products. Isopropyl alcohol and nitric acid (70%, used as received) were purchased from Sigma-Aldrich. Sulfuric acid (96%) and hydrogen peroxide (30%) were obtained from J. T. Baker. Piranha solution, for cleaning glass substrates consisted of 1:4 ratio (by volume) of hydrogen peroxide and sulfuric acid. For the glass substrate tested, thin (0.15 mm-thick) glass coverslips (12 mm-diameter) were purchased from Electron Microscopy Sciences.

Sample Preparation and characterization: Bare silicon wafers and glass coverslips were cleaned by oxygen plasma exposure (Harrick Plasma Cleaner) for 60 seconds at 10 W and subsequently immersed in freshly-prepared piranha solution for 10 minutes. The substrates were then rinsed using deionized (DI) water and dried under nitrogen. For the glass samples, PDMS stencil masks with 5 mm-diameter spots were prepared using a laser cutter (VersaLaser, Universal Laser System). The stencil masks were then cleaned with isopropyl alcohol and dried under nitrogen flow. The Piranha-cleaned coverslips were aligned over the stencil with the sample surface facing the stencil. The stencil was then mounted onto a 4-inch wafer before being loaded into the sputtering machine (Kurt J. Lesker) for sequential deposition of metals. The piranha-cleaned silicon wafers were either cut into small pieces for blanket depositions or patterned by photolithography before being loaded into the sputtering machine. First, a 160 nm-thick chrome layer was sputtered at 300 W as an adhesive layer between the supporting substrate and the subsequent metal layers. Next, 80 nm of gold was sputtered at 400 W as a seed layer to reinforce the porous coating. Finally, silver and gold were co-sputtered at 100 W and 200 W respectively. All depositions were performed under argon atmosphere at 10 mTorr. All films fabricated for this study presented a final stack size of ~1 micrometer and an alloy thickness of ~600 nm. Prior to dealloying the precursor AuAg alloy to produce np-Au films, the samples were treated with oxygen plasma for 60 seconds at 10 W and then immersed in heated nitric acid for 15 minutes at 55 °C. Following dealloying, samples were rinsed with DI water three times and stored in DI water for one day before drying under nitrogen flow and storing in Parafilm sealed dishes. Top view images of samples were thresholded using a custom ImageJ (NIH freeware) macro and subsequently analyzed using custom MATLAB and Python scripts to quantify morphological differences between films through comparing average ligament width and pore areas. Briefly, the

gray-scale SEM images were segmented into monochrome images in order to define pore as black and ligaments as white. A MATLAB script was then used to calculate the average width of the white features (ligaments) where as Python script was used to edge find the black features (pores) to calculate the pore areas.

Finite Element Thermal Modeling: COMSOL 4.4 was used to construct a 2D axisymmetric model of a circular np-Au sample being irradiated with a 5 μm laser spot. The geometry used for the model is demonstrated in Figure S1 and a comprehensive list of parameters used in the simulations is shown in Table S1.

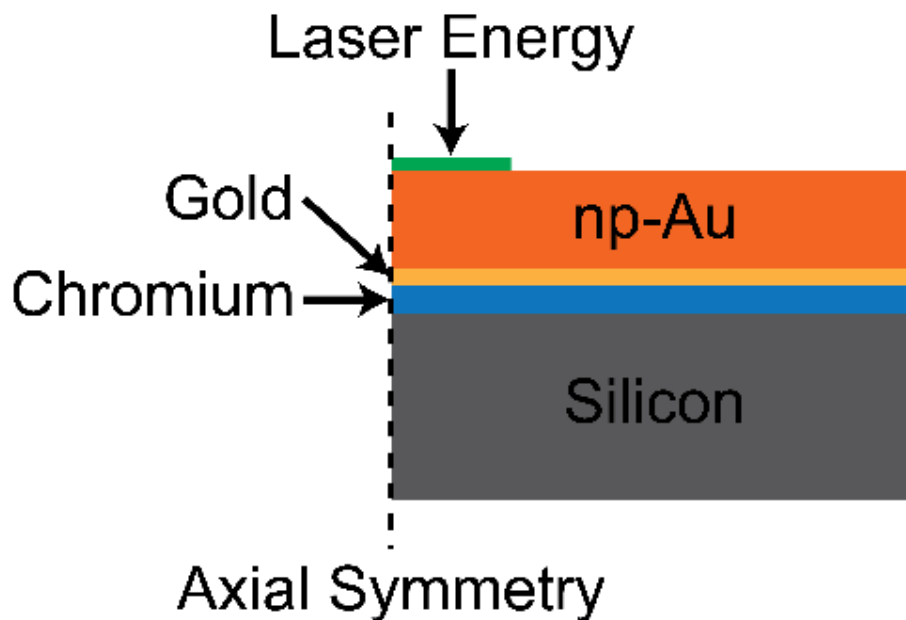


Figure S1. The geometry of the model used for this study was built through a 2D axisymmetric revolution around the origin with the laser energy focused at the origin at the middle of the sample.

Table S1. Parameters Used in np-Au Film Temperature Simulation

Parameter	Symbol	Value
<i>CW</i>		
Laser spot diameter	d	5 μm
Laser power	E_{cw}	2.54 – 5.09 MW/cm ²
Exposure duration	τ_{cw}	10 ms
<i>Pulsed</i>		
Laser spot diameter	d	8 μm
Pulse energy	E_{p}	0.025 J/cm ² – 0.25 J/cm ²
Pulse duration	τ_{p}	9 ns
Firing frequency	f	50 Hz
<i>Material Properties</i>		
Base temperature	T_{o}	300 K
Thermal conductivity of np-Au	$\kappa_{\text{np-Au}}$	67.14 W m ⁻¹ K ⁻¹
Emissivity of np-Au	$\epsilon_{\text{np-Au}}$	0.47
Reflectivity of np-Au	$R_{\text{np-Au}}$	0.22
Thermal conductivity of silicon	κ_{Si}	149 W m ⁻¹ K ⁻¹
Thermal conductivity of chromium	κ_{cr}	93.9 W m ⁻¹ K ⁻¹
Thermal conductivity of bulk gold	$\kappa_{\text{pl-Au}}$	317 W m ⁻¹ K ⁻¹
Thermal conductivity of glass	κ_{glass}	1.47 W m ⁻¹ K ⁻¹
Thermal conductivity of air	κ_{air}	COMSOL modeled

<i>Material Geometries</i>		
Silicon thickness	h_{si}	500 μm
Chromium adhesion layer thickness	h_{cr}	50 nm
Gold seed layer thickness	h_{au}	80 nm
Np-Au film thickness	$h_{\text{np-Au}}$	600 nm
Air thickness	h_{air}	4 μm

Custom Laser Annealing System: The custom continuous-wave photothermal annealing set-up was constructed at LLNL and a detailed schematic of the setup is seen in Figure S2 below. The LabVIEW program used to control the system was custom written and able to control XY stage movement, both Basler CCD and Mikrotron high framerate cameras for visualizing laser spot and the sample surface as well as control the laser power and shutter.

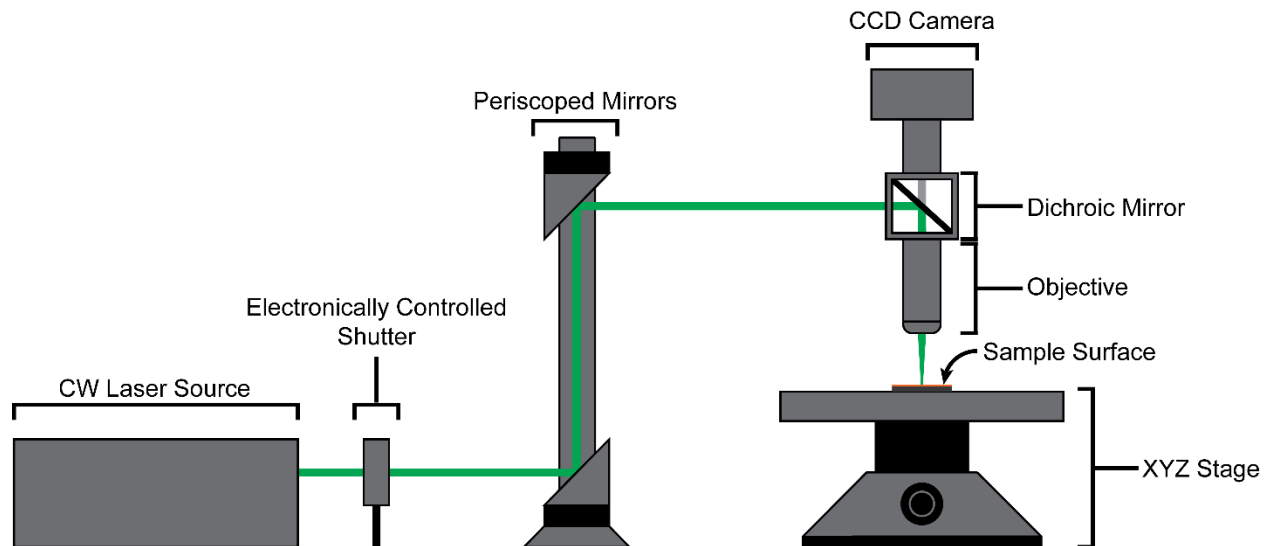


Figure S2. Schematic of CW photothermal annealing set-up used to anneal np-Au coatings.

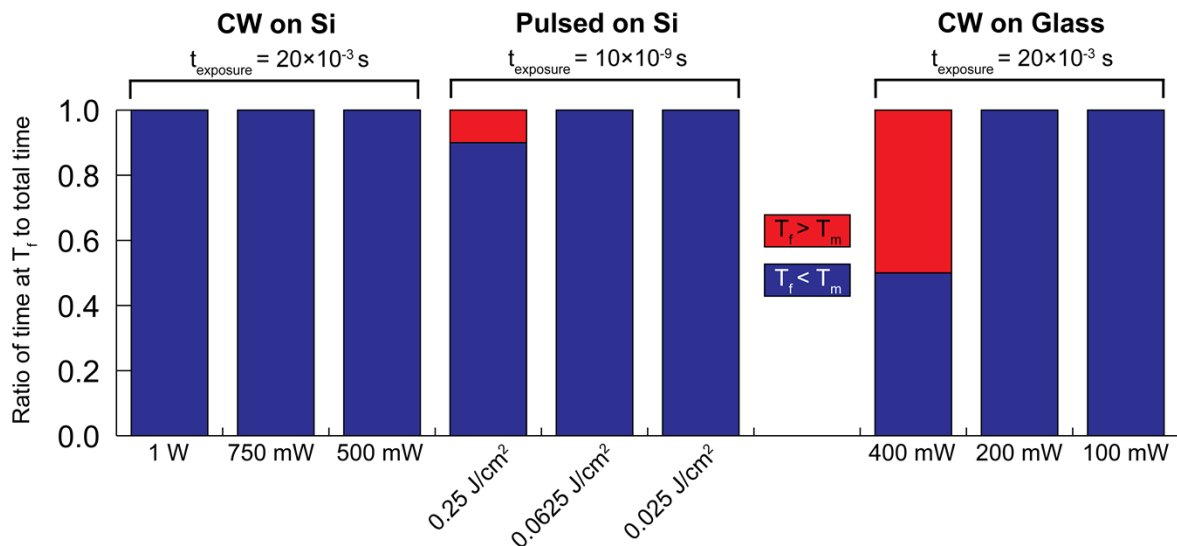


Figure S3. Graphical depiction of the exposure time of a treated film at temperatures below and above the melting point of bulk gold (1337 K) during photothermal annealing with each laser mode and supporting substrate.

Smoothing Dynamics of np-Au: Many models exist to capture both the viscous and diffusion related rearrangement of nanostructured surfaces in an analytical model. Therefore, it is possible to qualitatively validate that this difference in morphology is stemming from pulsed irradiation leading to viscous flow of np-Au, whereas surface atom diffusion is the dominating mechanism in CW irradiation. Cassidy et al.¹ posit a simple model for the general smoothing kinetics of uniformly repeating structures on glass, which can be viewed as a simple structural model for np-Au. Briefly, the time course function of the changing surface structure due to surface diffusion and capillarity is a function of the Fourier space power spectrum given by

$$C_n(t) = C_n(0) \exp \left[- \left[B(n\omega)^4 + F(n\omega) \right] t \right]$$

where $C_n(t)$ and $C_n(0)$ are the power spectral density functions from the 2D Fourier transform of the ending and beginning surface morphologies respectively, B is the scaling factor for surface atom diffusion smoothing and F is the scaling factor for capillary (viscous) flow smoothing.

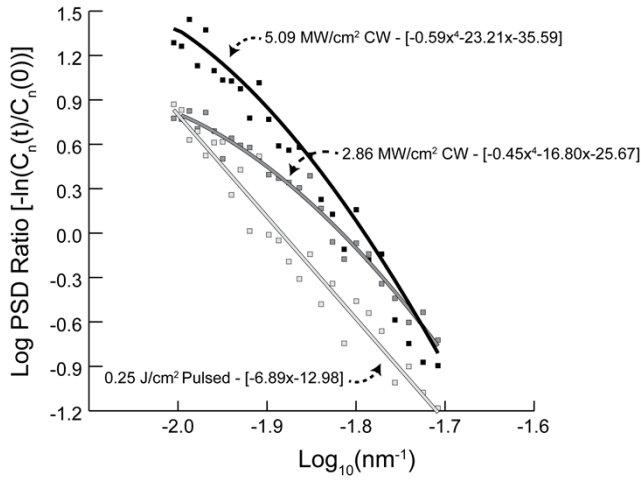


Figure S4. Log ratio of power spectral density (PSD) function further suggests differences in the smoothing dynamics between CW and pulsed mode annealing. Fit equations are given in square brackets and show clear differences in smoothing mechanisms between the two laser modes.

Plotting the natural log of the PSD ratio between samples annealed with CW and pulsed irradiation and their original starting morphologies reveals that pulsed mode behaves in a mostly linear regime (characteristic of capillary flow) for the entirety of the spatial frequencies tested, whereas CW annealing introduces a quartic relationship (characteristic of surface diffusion) to the smoothing model (Figure 5). This supports the previous observations that the pulsed mode

irradiation leads to coarsening mostly through bulk viscous flow of the Au in the np-Au film and not through surface atom diffusion.

Effect of Increased Reflectivity on Film Temperature:

Heating Profile and Temperature Distributions for Bulk Au Reflectivity ($R_{pl-Au} = 0.62$) np-Au (40% Increased Reflectivity)

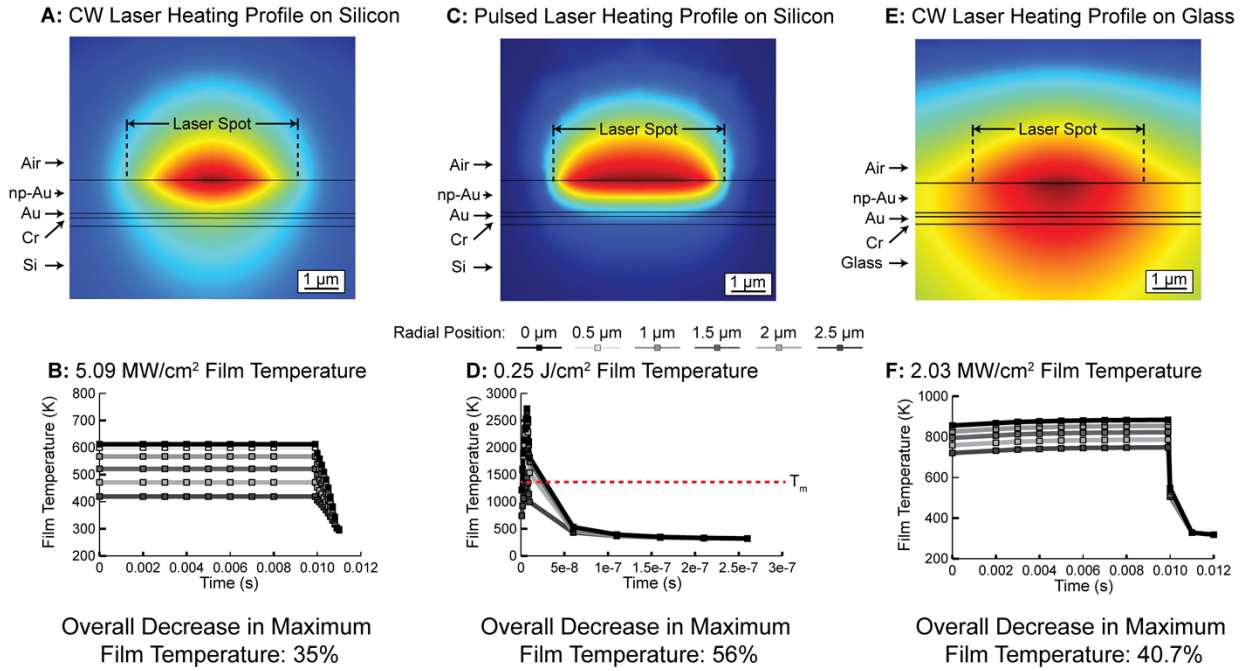


Figure S5. Simulated heating profile and film temperatures for CW (A) and pulsed (C) on silicon as well as CW on glass (E) accounting for a reflectivity change to that of bulk Au demonstrate an overall decrease in temperatures for all modes and substrates (B,D,F).

Effect of Increased Thermal Conductivity on Film Temperature:

Heating Profile and Temperature Distributions for 200 nm Ligament Diameter np-Au
(41.6% Increased Thermal Conductivity)

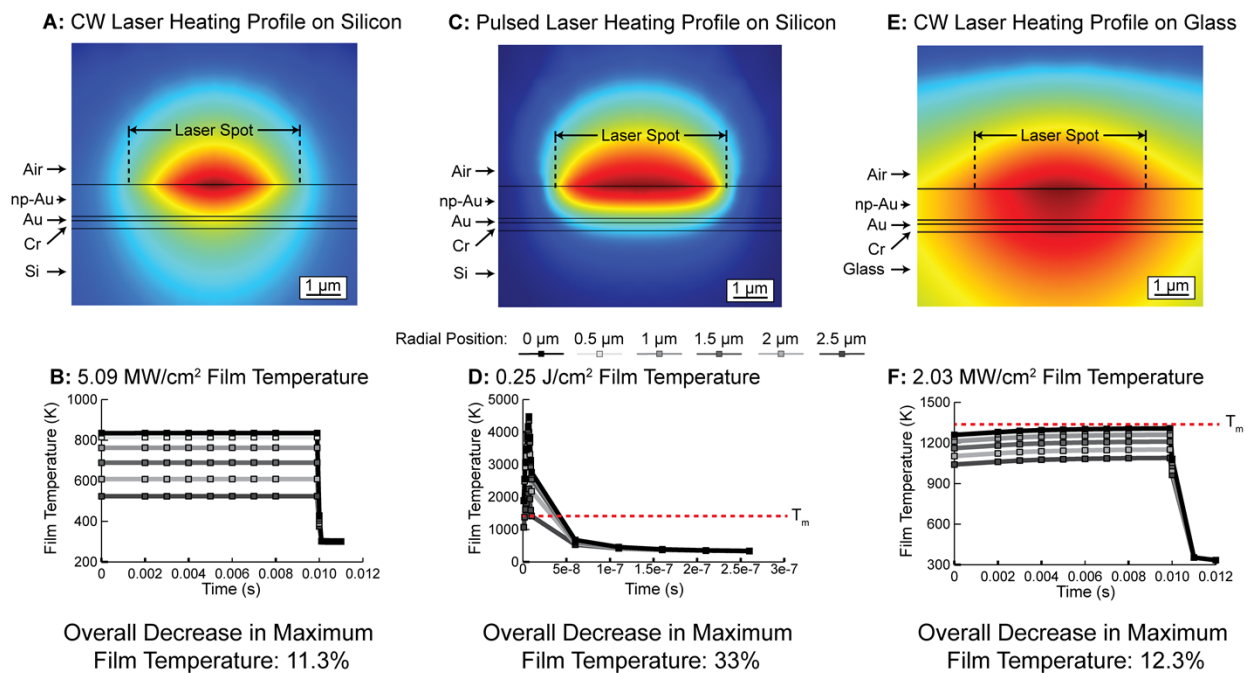


Figure S6. Simulated heating profiles and film temperatures for CW (A) and pulsed (C) on silicon as well as CW on glass (E) accounting for a thermal conductivity change to that of np-Au with a 200 nm ligament diameter demonstrate an overall decrease in temperatures for all modes and substrates (B,D,F). Because of the short temporal exposure, pulsed mode irradiation suffers from almost three times the reduction in film temperature than CW mode.

References:

1. Cassidy, D. C. G., N. A., Capillarity-Induced Smoothing of Glass Surfaces by Viscous Flow. *J. Am. Ceram. Soc.* **1969**, 53, 161-168.